Anti-thermal quenching in Nd^{III} molecular near-infrared thermometers operating at physiological temperatures

Check for updates

María José Maldonado[1], Patricia Farías-Carreño[1], Yolimar Gil[1], Andrés Vega[2], Ricardo Costa de Santana [3], Daniel Aravena [4]✉, Carlos D. S. Brites[5], Luís D. Carlos [5], Albano N. Carneiro Neto [5]✉, Fiorenzo Vetrone[6] & Pablo Fuentealba [1]✉

Examples of molecular complexes acting as thermometers operating at room temperature in near infrared region are scarce, therefore this work showcases the anti-thermal quenching effect on neodymium(III) molecular thermometers working in biological windows within the physiological temperature range. A mononuclear complex, [Nd(L)(NO$_3$)$_3$] (**1Nd**), where L is a macrocyclic ligand, was synthesized and used as a precursor to develop two novel species: a dinuclear, [(Nd(L)(NO$_3$))$_2$(μ-BDC)] (NO$_3$)$_2$·H$_2$O (**2Nd**), linked by 1,4-benzenedicarboxylate (BDC), and a hexameric, [(Nd(L))(μ-BTC) (H$_2$O)]$_6$·35H$_2$O (**6Nd**), linked with 1,3,5-benzenetricarboxylate (BTC). Thermometric properties were studied in the physiological temperature range (292-332 K), utilizing 804 nm laser excitation (first biological window) and monitoring emissions in the second biological window (908, 1065, and 1340 nm) associated with the $^4F_{3/2} \rightarrow {}^4I_{9/2}$, $^4I_{11/2}$, $^4I_{13/2}$ transitions, respectively. Among the complexes, the hexamer **6Nd** exhibited exceptional performance, with S_r of 2.4%K^{-1} at 293 K, when luminescence intensity ratio (LIR) of two Stark components of the $^4F_{3/2} \rightarrow {}^4I_{11/2}$ emission was used, positioning it as a high-performance Nd^{III}-based thermometer. All complexes displayed anti-thermal quenching behavior, surpassing the current molecular-based thermometers in the near-infrared region. Theoretical calculations using complete active space self consistent field (CASSCF) and Boltzmann population models between Kramers doublets of the $^4F_{3/2}$ level were performed to rationalize the anti-thermal behavior.

Physiological temperature is critical for thermometric applications because it plays a role in thermoregulation, the body's ability to maintain a stable internal temperature despite environmental changes. Thermoregulatory physiology keeps the core temperature around 37 °C, which is essential for normal cellular function. Disruptions in thermoregulation can lead to conditions like hypothermia (below 35 °C) or hyperthermia (above 40.5 °C), both of which can have serious health consequences. Thus, precise temperature monitoring is essential for detecting impairments in thermoregulatory pathways, such as in conditions affecting the autonomic nervous system, and for preventing life-threatening outcomes[1]. Accurate temperature measurement within the physiological range is vital for early detection

and intervention in these potentially dangerous states, supporting the importance of new thermometric technologies in medical diagnostics and treatment.

The lanthanides have revolutionized materials science due to their proven applications in different areas, such as magnetism[2–4], catalysis[5], and optoelectronics[6,7]. Such distinctive properties arise from their electronic configuration, where the valence electrons lie in the well-shielded 4f orbitals[8]. The trivalent lanthanide ions are known for their narrow emission bands that span the ultraviolet (UV), visible, and near-infrared (NIR) regions, associated with long lifetimes of the emitting states. These optical properties are exploited for many applications in optoelectronics, lighting,

[1]Facultad de Ciencias Químicas y Farmacéuticas, Universidad de Chile, Santiago, Chile. [2]Departamento de Ciencias Químicas, Universidad Andrés Bello, Santiago, Chile. [3]Instituto de Física, Universidade Federal de Goiás, Campus Samambaia, Goiânia, GO, Brazil. [4]Departamento de Química de los Materiales, Facultad de Química y Biología, Universidad de Santiago de Chile, Santiago, Chile. [5]Physics Department, CICECO–Aveiro Institute of Materials, University of Aveiro, Aveiro, Portugal. [6]Institut National de la Recherche Scientifique, Centre Énergie, Matériaux et Télécommunications, Université du Québec, Varennes, Montréal, QC, Canada. ✉e-mail: daniel.aravena.p@usach.cl; albanoneto@ua.pt; pfuentealbacastro@ciq.uchile.cl

LEDs, among others, particularly from cations emitting in the visible region, such as Eu^{III}, Tb^{III}, and Dy^{III} [9].

Pioneering work in this area was developed in the visible range. However, other applications in telecommunications and biology, utilize NIR emissive cations, such as Nd^{III}, Er^{III}, or Yb^{III}, among others[10,11]. For the latter, NIR emission (and excitation) is vital since many biological species can fluoresce under high-energy (UV or visible) excitation, causing unwanted autofluorescence[12]. Moreover, NIR radiation within biological windows (BW) (BW-I: 650–950 nm; BW-II: 1000–1350 nm, and BW-III: 1550–1870 nm) offers deeper tissue penetration, enhanced image contrast, and reduced phototoxicity, making it a rapidly expanding field of study[13]. In this regard, lanthanide-based materials present key advantages, since some of their absorption and emission bands lie in these regions.

Among the lanthanide ions, Nd^{III} is most advantageous since it can be directly excited in the first BW with 804 nm radiation, inducing emission in the second BW with bands centered at 908, 1065, and 1340 nm, arising from transitions between the $^4F_{3/2}$ excited state to the lower $^4I_{9/2}$, $^4I_{11/2}$, and $^4I_{13/2}$ states, respectively[14,15]. Furthermore, the energy gap between some of the Nd^{III} excited states, such as the $^4F_{7/2}$ and $^4F_{5/2}$ states as well as the $^4F_{5/2}$ and $^4F_{3/2}$ states, have an energy gap close to 1000 cm^{-1}, which are known as thermally coupled levels, that are useful for luminescence thermometry as the intensity of these two bands changes as a function of temperature (known as luminescence intensity ratio (LIR) thermometry)[16]. It is important to mention that in Nd^{III}-based systems, it is also possible to evaluate thermometric performance by analyzing the behavior of a single band using the LIR of the individual Stark levels[17].

Emissive transitions from the $^4F_{7/2}$ and $^4F_{5/2}$ states give emission bands that lie in the first BW, while from $^4F_{3/2}$ it is also possible to obtain valuable information in the second BW, being an advantageous factor in avoiding excitation laser interference. This cation has been studied for luminescence thermometry in different luminescent materials, such as mononuclear complexes, nanoparticles, glasses, and some MOFs[18–21]. However, unlike inorganic nanomaterials, Nd^{III}-based complexes are on size scales similar to those of biological molecules and thus can further extend the application of luminescence thermometry. Furthermore, it should be possible to incorporate ligands (L) interacting with biological systems, allowing us to investigate how temperature affects basic biological functions.

In lanthanide coordination compounds, modifications in the chemical environment influence the electronic structure of the cation giving rise to different Stark splitting[22], which can be evidenced by optical spectroscopy and hence exploited for thermometry. Thus, molecular complexes are highly versatile platforms and can be easily tuned by modulating the crystal field of the cation, using different L, or synthesizing complexes with different nuclearities. Molecular thermometry has been explored by different researchers, where most of the work is focused on the visible range emitting cations[23]. In this area, remarkable results have been obtained, such as proper connectivity between emitting ions to modulate intermetallic energy transfer[24,25], which have promoted improvements in thermal sensing. Despite all these interesting aspects, there are not many examples in the literature focused on the analysis of the thermometric performance of coordination compounds in the physiological temperature range operating in the BWs.

Anti-thermal quenching is a good approach to enhance the performance of luminescent materials, particularly in high-temperature applications[26]. This phenomenon arises because increased thermal energy can lead to non-radiative relaxation processes, which diminish the material's luminescence efficiency. To avoid thermal quenching, strategies, such as incorporating energy reservoirs like Frenkel defects, optimizing host materials to resist thermal degradation, and employing controlled defect engineering have been developed[27]. These methods help to mitigate the loss of luminescence and maintain or even improve performance under elevated temperatures.

In this article, we have explored the NIR thermometric properties of three novel Nd^{III} complexes within the physiological temperature range, by using 804 nm excitation that lies in the first BW. The influence of the first coordination sphere in the Stark splitting of the $^4F_{3/2} \rightarrow {}^4I_{11/2}$ transition was evidenced by the electronic structure obtained from theoretical calculations. Interestingly, the three compounds showed anti-thermal quenching effects, which allows an increase in the population of the $^4F_{3/2}$ level, improving their thermometric performance. A thermal sensitivity of 2.4%K^{-1} at 293 K was obtained for the hexanuclear complex (**6Nd**) by using the LIR of two components of narrow $^4F_{3/2} \rightarrow {}^4I_{11/2}$ transition. Therefore, these results open the doors to using the anti-thermal quenching effect for boosting thermometric behavior in molecular systems and demonstrate the potential for Nd^{III}-based systems in practical applications.

Methods
Experimental
The details of synthesis of the mononuclear ([Nd(L)(NO$_3$)$_3$], **1Nd**)[28–31], the dinuclear [(Nd(L)(NO$_3$))$_2$(μ-BDC)](NO$_3$)$_2$·H$_2$O, **2Nd**), and the hexameric ([(Nd(L))(μ-BTC)(H$_2$O)]$_6$·35H$_2$O, **6Nd**) complexes are in the Supporting Information. BDC and BTC correspond to the 1,4-bencenedicarboxylate and 1,3,5-bencenetricarboxylate, respectively.

FTIR spectra of the synthesized compounds were collected using a SpectrumTwo spectrophotometer from Perkin Elmer, coupled with an attenuated total reflectance accessory from PIKE Instruments. CHN analyses were performed on a Thermo Scientific Flash 2000 elemental analyzer. Thermal analysis was performed using an Iris TG209 from Netzsch. Data were collected from room temperature to 1273 K using a 10 K/min heating ratio in nitrogen atmosphere. Diffuse reflectance spectra were recorded on a UV-Vis PerkinElmer Spectrometer, model Lambda 35, coupled with an RSA-PE-20 integration sphere from LabSphere, while emission spectra were recorded using on a Horiba-Jobin Yvon spectrofluorimeter, Model Fluorolog-3 (FL3-221), using an 804 nm laser. Deconvolution of transition intensities $I(\lambda)$ was done considering two peaks and using a Gaussian-type function: $I(\lambda)=I_0 + [A/(w\sqrt{(\pi/2)})]exp(-2[(\lambda-\lambda_0)/w]^2)$, where I_0 represents the baseline intensity, A is the amplitude of the peak, λ_0 is the barycenter, and w is the full width at half maximum of the Gaussian peak.

X-ray diffraction datasets for **1Nd**, **2Nd**, and **6Nd** were collected on a SMART-APEX II CCD diffractometer at room temperature. Data were reduced using SAINT[32], while the structure was resolved by direct methods, and subsequently completed by difference fourier synthesis and then refined by least-squares using SHELXL[33]. Multi-scan or numerical absorption corrections were applied using SADABS[32]. The hydrogen atoms were calculated at idealized positions after each cycle with SHELXL using a riding model, with C–H distance of 0.93 and 0.96 Å for aromatic and alkyl hydrogen atoms, respectively. $U_{iso}(H)$ values were set equal to 1.2U_{eq} of the parent atoms. During the last stages of structure completion of **2Nd**, it was evident that the structure should contain counterbalancing nitrate anions and solvent molecules in the inter-cationic space, but efforts to refine them as disordered positions failed. Considering this failure, we chose to use SQUEEZE[34,35], a well-known and documented method for the modeling of ill-defined electron density, to consider the effect of the disordered anions and solvents. During the final refinement stages, the effect of the solvent and anions were considered by this means. It is important to note that the use of SQUEEZE has practically no effect on any structural parameters of the molecule. The formula was established based on elemental analysis and thermogravimetric analysis. Table S1 shows the main data collection and refinement details for each compound, which were prepared with the help of public CIF[36]. Table S2 presents selected bond lengths and angles for the molecules studied.

Theoretical
Electronic structure calculations were carried out by means of the ORCA 5.0.4 program[37], CASSCF(3,12)[38] calculations considered an active space composed by the 4f and 5d shells, in which 35 quartets were requested. Scalar relativistic effects were described by the DKH Hamiltonian[39]. The basis set for light elements was def2-TZVP[40] and the basis for Nd was SARC2-DKH-QZVP[41]. CASSCF calculations are expected to overestimate interelectronic repulsion, while spin-orbit and L field effects are better

described under this methodology[42]. To correct this shortcoming while maintaining the SOC and L field description of CASSCF, calculations were performed for the Nd^{III} free ion, which allowed us to construct an effective Hamiltonian where the calculated Racah parameters are replaced with reference spectroscopic data[43].

Comparing the CASSCF calculations of **1Nd, 2Nd**, and **6Nd** and the corrected and uncorrected results for the free ion allows to derive the energetic correction due to the change in the Racah parameters. The luminescence spectrum was approximated assuming $I \propto E^4$ $(\mu^2 + m^2 + Q^2)$, following refs. 44,45, and the populations of the two doublets associated with the $^4F_{3/2}$ multiplet were weighted according to a Boltzmann distribution.

The mononuclear models for **2Nd** and **6Nd** were constructed from their crystallographic structure. In the case of **2Nd**, the L coordinated to one of the Nd^{III} ions were retained intact. In the case of **6Nd**, the environment of Nd^{III} consisted of the belt macrocycle, one water L, and two BTC L, where the hydrogen positions were optimized using the BP density functional[46,47]. To avoid convergence problems in hydrogen optimization, the Nd^{III} center was replaced by Y^{III} described with electron core potentials[48] and the Def2-TZVP basis set[40].

Results and discussion
Structural description and characterization

The three coordination compounds were characterized by single-crystal X-ray diffraction. The crystallographic data summarized in Table S1 reveals that these complexes crystallize in the monoclinic C2/c (**1Nd**), orthorhombic Fddd (**2Nd**), and trigonal R$\bar{3}$ (**6Nd**) space groups. For the three complexes, the macrocyclic L is coordinated to the Nd^{III} ions through the six donor nitrogen atoms as is shown in Fig. 1a. **1Nd** is a mononuclear complex with a Nd^{III} ion dodecacoordinated featuring a N$_6$O$_6$ coordination environment, where in addition to the macrocyclic L, three bidentate nitrate anions are coordinated to the metal center, where two of them are above and one below the macrocycle plane (Fig. 1b). For **2Nd**, the data reveals a dinuclear complex where both Nd^{III} ions are decacoordinated with an N$_6$O$_4$

coordination sphere (Fig. 1c). Each Nd^{III} ion is coordinated to a macrocycle L and both centers are connected by the BDC anion through two oxygen atoms of the carboxylate moiety. Perpendicular to this bridging L, a bidentate nitrate anion completes the first coordination sphere, and two non-coordinated nitrate anions neutralize the positive charge of this complex. The 2,5-pyridilen moieties on the macrocyclic rings define stack interactions in the solid as depicted in Fig. S1 (ipd: 3.355(2) Å and CCD: 3.583(2)).

For the hexameric **6Nd**, six units of (NdL)$^{3+}$ are linked by six BTC^{3-} bridging L through two of the three carboxylate groups (Fig. 1d). As the repetitive units have the same charge, **6Nd** corresponds to a neutral compound. Each of the six Nd^{III} centers is decacoordinated exhibiting an N$_6$O$_4$ coordination sphere, where aside from the macrocyclic L, a bidentate, and a monodentate carboxylate groups of BTC^{3-}, and a water molecule are coordinated to the metal ion. For major clarity, the repetitive unity is depicted in Fig. S2c.

To evaluate the coordination geometry of the Nd^{III} center, continuous symmetry measurement (CShM) values were calculated using the SHAPE 2.1 program[49] (Tables S3–S5). The lowest CShM value for **1Nd** (2.054), **2Nd** (1.811), and **6Nd** (1.470), indicates that these complexes can be described as an icosahedron when twelve coordinated as in **1Nd** and a tetradecahedron (2:6:2) for complexes **2Nd** and **6Nd**, where both compounds present the Nd^{III} center with a ten-coordinated environment.

With regards to the characterization of **1Nd** performed by FTIR spectroscopy (Fig. S3), it is important to highlight the vibration band due to the imine group at 1654 cm^{-1}, which proves the successful condensation reaction. The bands observed at 2915 and 1590 cm^{-1} are due to the ethylene and pyridine moieties, respectively. Vibration bands due to nitrate ions are observed at 1450, 1300, and 1030 cm^{-1}. These bands are associated with nitrate L with a bidentate coordination mode, in agreement with the structure obtained by X-ray diffraction.

A broad band above 3000 cm^{-1} is observed in the FTIR spectra of the **2Nd** due to the presence of water molecules. Aside from the vibration bands

Fig. 1 | Crystallographic structure for all presented complexes. a Coordination of the macrocyclic ligand (L) and **b** the molecular structures for **1Nd**. The molecular structure of the **c** dimeric **2Nd** and **d** the hexameric **6Nd** compounds. Hydrogen atoms were omitted for clarity.
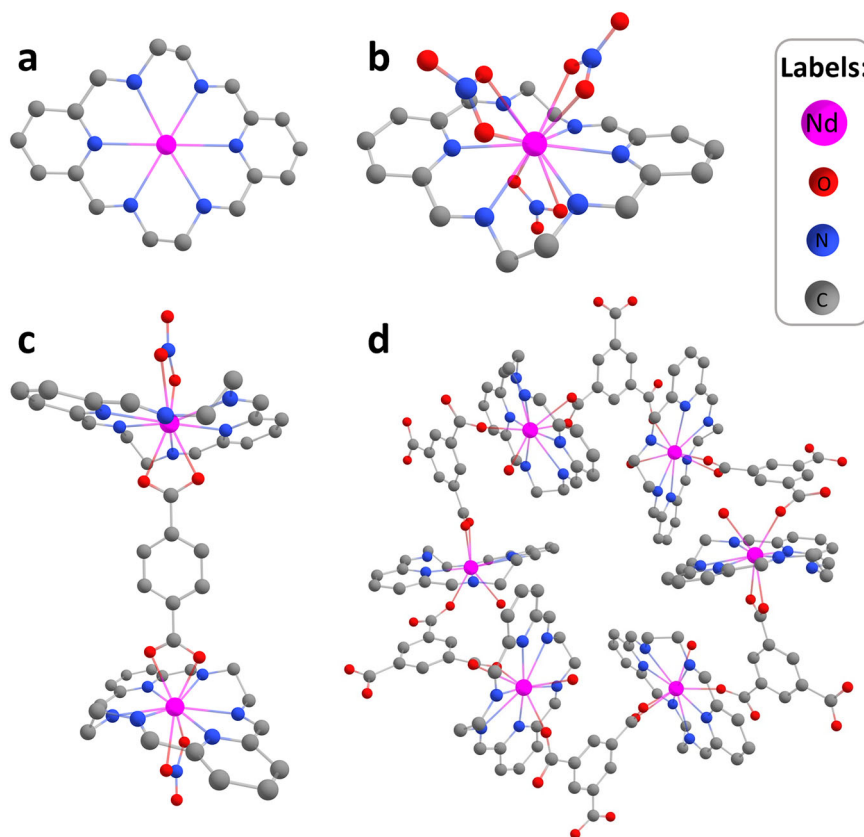
due to the macrocyclic L at 1657 and 1559 cm^{-1} due to imine and pyridine groups, additional bands were detected at 1533 and 1506 cm^{-1}, which are assigned to the carboxylate units and aromatic ring of the BDC bridging L. The band at 835 cm^{-1} is characteristic of the *para* substitution of the benzyl ring of the linker[50]. The spectrum also shows a band at 1383 cm^{-1} attributed to the anionic nitrate ions.

For compound **6Nd**, vibrations due to the macrocyclic L are found at 1657 and 1607 cm^{-1}, and bands due to BTC linker are present at 1550–1537 cm^{-1} due to carboxylate groups, while the band at 760 cm^{-1} is attributed to the ν(C-H) of 1,3,5-substituted benzene ring[51]. In this case, no bands due to nitrate ions are observed, consistent with the full replacement of these species, as described in the crystallography section.

From the thermal analysis (Fig. S4) it is important to mention that the obtained species are stable in the physiological temperature range, which was used to evaluate the thermometric properties in the present study. Compound **1Nd** is anhydrous, as established by *X*-ray diffraction and confirmed by thermal analysis. This complex shows an abrupt mass loss near 563 K due to the decomposition of bidentate nitrate ions. This step represents a higher mass percentage than that calculated for only the three nitrate anions, which may be attributed to partial decomposition of the macrocyclic L since this is followed by a permanent mass loss until 1273 K. (Fig. S4)

On the other hand, complex **2Nd** contains crystallization water molecules, evidenced by FTIR and by the mass loss below 373 K. A continuous mass loss is observed from 373 to 523 K, which may be attributed to the nitrate counterions present in the crystalline lattice. Another decomposition step takes place at 553 K, which should be attributed to the remaining bidentate nitrate ions, due to the similar decomposition temperature observed for **1Nd**. Finally, above 573 K, a continuous weight loss is evidenced that should include the decomposition of the BDC linker and the macrocyclic L.

For compound **6Nd**, three main decomposition stages can be distinguished. The first one corresponds to the loss of crystallization water molecules, similar to the profile observed for **2Nd**. In this case, a much higher quantity of water content was found, which is explained by two factors: i) uncoordinated carboxylate groups, which are stabilized by water molecules, and ii) the cavity formed by the hexameric unit which should allow a higher hydration content as compared with **1Nd** and **2Nd**. A second decomposition is observed ca. 508 K, which is due to coordinated water molecules. Finally, a continuous mass loss is evidenced above 593 K that should include the decomposition of the bridging BTC and the macrocyclic L. It is important to remark that decomposition observed for **1Nd** and **2Nd** at 553 K assigned to nitrate ions is absent, in agreement with previous characterization techniques.

Optical properties

Solid-state diffuse reflectance spectra are depicted in Fig. S5. A broad band is observed below 350 nm ascribed to the absorption of the macrocyclic L. In the corresponding spectrum of the dimer **2Nd**, a second broad absorption band is detected at 420 nm, which may be attributed to the BDC bridging L. Furthermore, in the hexameric unit **6Nd**, this latter band expands to lower energies, almost overlapping the weak absorption band above 500 nm. Narrow bands were observed for the three complexes, due to the direct absorption transitions of the Nd^{III} ion, originating from the $^4I_{9/2}$ ground state to various 4f excited states (see Fig. S5 and Table S6)[52]. It should also be noted that the presence of the bands ca. 800 nm, due to the $^4I_{9/2} \rightarrow {}^4F_{5/2} + {}^2H_{9/2}$ transition, is of great importance since this wavelength is used to excite the Nd^{III} center in the first biological window and is used to evaluate the thermometric performance.

Having analyzed the absorption spectra for all coordination compounds, the photoluminescence spectra of the studied species were recorded. By using an 804 nm laser, it was possible to detect the corresponding narrow emission bands in the second BW. Figure 2 shows the representative spectra for the three complexes at room temperature. The emissive pathway involves the direct excitation of the $^4F_{5/2}, {}^2H_{9/2}$ mixed energy level, which
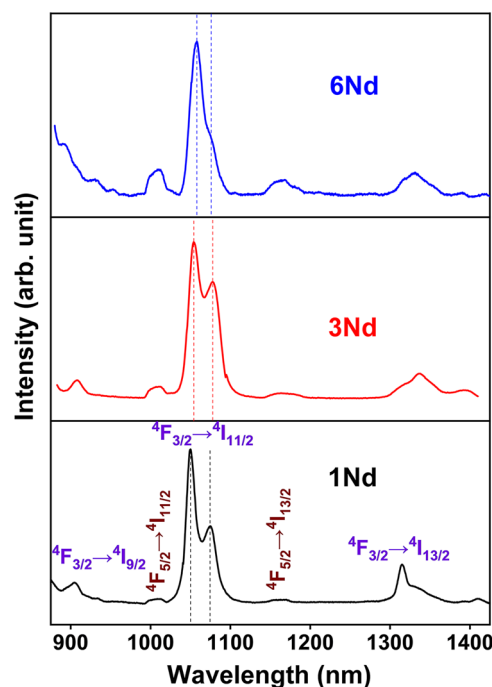

Fig. 2 | Emission spectra for the three complexes at 298 K, upon excitation with 804 nm laser. Dashed lines are guides for the barycenter of the two components of main transition $^4F_{3/2} \rightarrow {}^4I_{11/2}$, which will be further used in the analysis.

consequently populates the lower-lying $^4F_{3/2}$ level by non-radiative decay and thus leads to the observed emissions[53].

The $^4F_{3/2} \rightarrow {}^4I_{11/2}$ band is convenient for luminescence thermometry since its profile and intensity can be modulated by the local environment, covering a narrow section of the spectra in the second BW[54]. Furthermore, its splitting has been associated with the energy span of the two doublets stemming from $^4F_{3/2}$[15]. The deconvolution of the main band was done by fitting the plot of intensity vs cm^{-1}, as shown in Fig. S6, and the results of fittings are shown in Tables S7–S9.

Figure 3 shows the temperature-dependent emission spectra for the **6Nd** complex within the physiological temperature range, while similar spectra for **1Nd** and **2Nd** are presented in Fig. S7. These figures highlight the temperature-dependent emission of the $^4F_{5/2} \rightarrow {}^4I_{11/2}$ transition. Notably, **6Nd** is unique among the samples, as the $^4F_{5/2} \rightarrow {}^4I_{11/2}$ intensity decreases with increasing temperature, suggesting the presence of an additional feeding channel to the $^4F_{3/2}$ level via multiphonon decay.

As mentioned above, it is useful to have a narrow energy range to avoid instrumental error. Figure S8 presents the integrated areas of the two components of the $^4F_{3/2} \rightarrow {}^4I_{11/2}$ transition (named A$_1$ for the higher energy component and A$_2$ for the second component), and the total area as a function of temperature, where is possible to observe a general increase in intensity with increasing temperature, attributed to the anti-thermal quenching effect. This anti-thermal quenching may be due to the suppression of non-radiative pathways[55].

As seen in Figure S8, the two components of compounds **1Nd** and **2Nd** have similar behavior, slightly increasing in intensity with the increase in temperature. However, the slight increase gives low S$_r$, ranging from 0.1 to 1.1%·K^{-1}. Interestingly, in **6Nd**, while A$_2$ slightly increases with temperature, from 8.6 to 11.0 (less than 0.3 times), A$_1$ increases from 1.5 to 4.1 (more than 2.7 times). This increment in A$_1$ yields a higher S$_r$ of 3.9%·K^{-1} at 293 K. Furthermore, as both components have different temperature dependencies, it is useful to analyze their LIR. Figure 4 shows the temperature dependencies of the LIR and corresponding S$_r$ values (the corresponding values for LIR and the linear fit are presented in Table S10). For **1Nd** and **2Nd**, the LIR of the two components of the $^4F_{3/2} \rightarrow {}^4I_{11/2}$ transition is not a useful thermometric parameter.
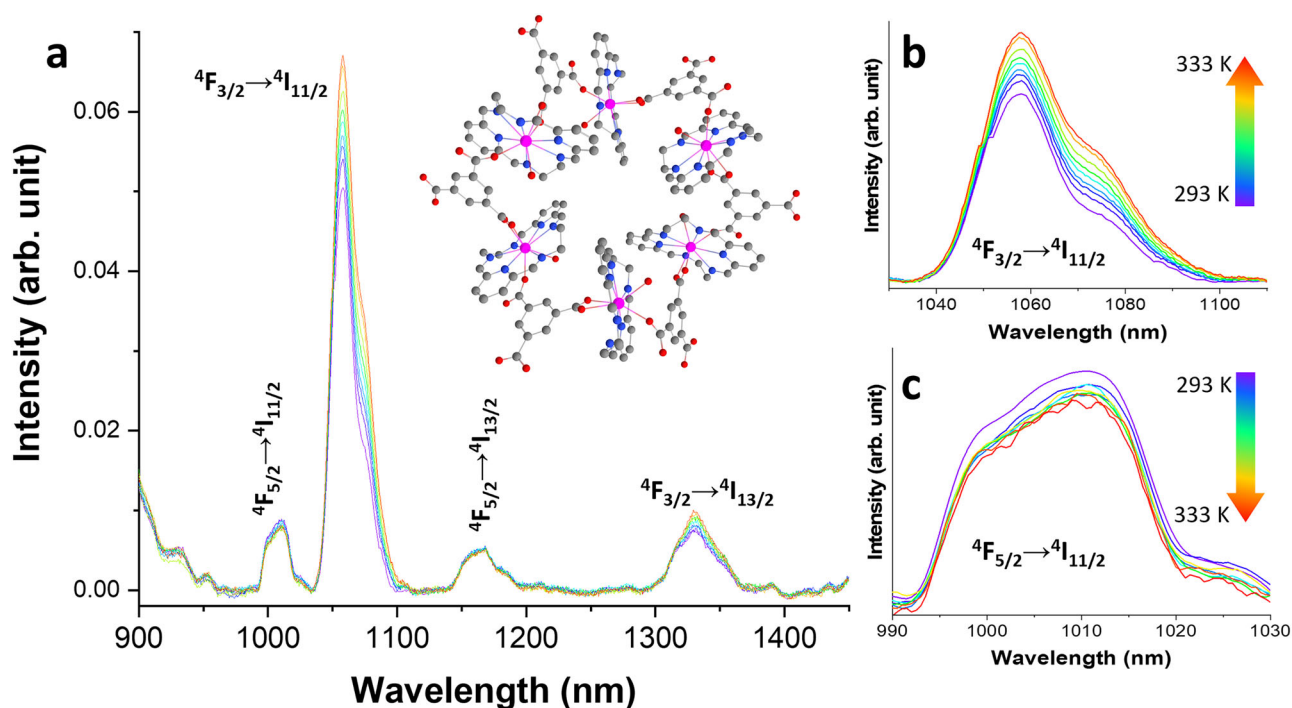
Fig. 3 | Temperature dependent emission spectra of the hexanuclear complex [(Nd(L))(μ-BTC)(H$_2$O)]$_6$·35H$_2$O (6Nd). a Displays the full emission spectrum, while **b** and **c** show the emissions corresponding to the $^4F_{3/2} \rightarrow {}^4I_{11/2}$ and $^4F_{5/2} \rightarrow {}^4I_{11/2}$ transitions, respectively. Spectra are presented from 293 to 333 K.

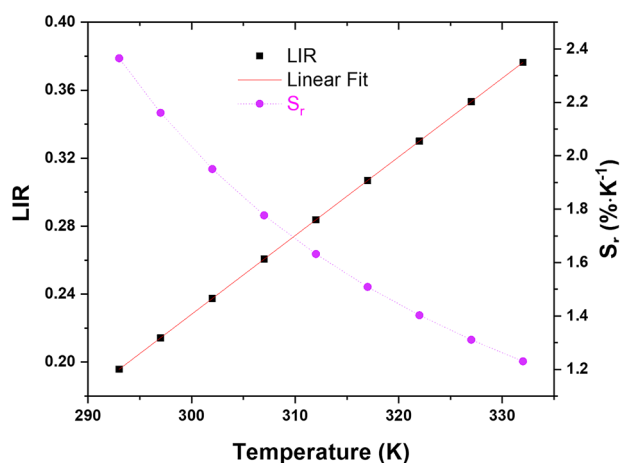**Fig. 4 | Temperature dependence of the LIR of the two components of the $^4F_{3/2} \rightarrow {}^4I_{11/2}$ transition for 6Nd and the respective relative thermal sensitivity values.** The full red line is the linear fit to the LIR data. The dashed line is a guide to the eyes.

From the LIR of the two components of **6Nd**, it is possible to observe a linear behavior that is desirable to thermometry. This parameter achieves a thermal sensibility of 2.4% · K^{-1} at 293 K, decreasing to 1.2% · K^{-1} at 333 K.

The thermometric performance of the samples was also investigated by analyzing the $(^4F_{3/2} \rightarrow {}^4I_{11/2})/(^4F_{3/2} \rightarrow {}^4I_{13/2})$ LIR. However, only complex **2Nd** presents a linear temperature dependence, with a low relative thermal sensibility of 0.1%·K^{-1}. Table 1 compares the thermometric performance of the complexes studied with that reported for other Nd^{III} coordination compounds.

Based on the data presented in Table 1, it can be concluded that **6Nd** is the most sensitive Nd^{III} compound reported to date, surpassing previous examples by at least one order of magnitude. This exceptional sensitivity suggests promising potential for future biological applications. Thus, this study underscores the significance of molecular complexes that may be effective molecular thermometers operating within the physiological

temperature range. To further enhance the thermometric properties of Nd^{III} complexes, future research should focus on developing species with varied nuclearities and alternative connectivities between metal centers.

Theoretical calculations

Electronic structure calculations were performed to grasp further details about the relation between the coordination environment and the shape of the $^4F_{3/2} \rightarrow {}^4I_{11/2}$ transition (see further technical details in the methods section). Figure 5 presents the calculated emission spectrum for **1Nd, 2Nd,** and **6Nd**. As expected from selection rules, calculations reveal that all emission bands associated with the $^4F_{3/2}$ multiplet are dominated by the electric dipole mechanism, so magnetic dipole and electric quadrupole contributions can be safely neglected. Focusing on the $^4F_{3/2} \rightarrow {}^4I_{11/2}$ transition, we observe a trend that is qualitatively consistent with results from Fig. 2, as two maxima are discernible in **1Nd** and **2Nd** and appear merged in the case of **6Nd**. The relative intensity of both maxima is not properly captured in all cases, as compound 2Nd shows its main peak at 1075 nm instead of a more intense signal at 1050 nm in comparison with the 1075 nm maximum.

Figure 6 shows the Dieke diagram of **6Nd** with the corresponding calculated spectra and the $^4F_{3/2} \rightarrow {}^4I_{11/2}$ transition decomposed in the intensity stemming from the lower and higher energy Kramers' doublets of the emissive multiplet (identified as Γ and Γ' in Fig. 6, respectively). Dieke diagrams for **1Nd** and **2Nd** are given in Figure S9. We observe the two-peak pattern for **1Nd** and **2Nd**, where the relative intensity of both maxima is dependent on the emissive state. In contrast, results for **6Nd** show a single peak signal, irrespective of the emissive doublet. As the Γ doublet is at slightly lower energy, the band for this doublet (dashed line in Fig. S10a) is shifted to lower energy in comparison with the intensity associated with the Γ' doublet (solid line in Fig. S10a). In any case, this splitting is significantly smaller than the energy difference of the two-peak pattern, suggesting that the origin of this separation is related to the splitting of the $^4I_{11/2}$ multiplet instead of $^4F_{3/2}$.

To corroborate this point, the splitting of the $^4I_{11/2}$ multiplet was analyzed in further detail. Interestingly, the Kramers' doublets tend to cluster in two groups for all cases, with an energy separation between barycentres in the order of 100–150 cm^{-1}, which is consistent with the observed

Table 1 | Summary of the thermometric performance and operating temperature range for Nd^III-based coordination compounds

Compound	Classification of emitter	Coord. Sphere	λ_{exc} (nm)	Operative temperature range (K)	Sr (%·K⁻¹) (T(K))	Thermometric parameter	Ref.
[Nd(phen)₃(NCS)₃]·0.3EtOH	Molecular (mononuclear complex)	N₉	355	150–300	0.2 (300)	LIR (1060/874 nm)	58
[Nd(phen)₃(NCSe)₃]·0.3EtOH	Molecular (mononuclear complex)	N₉	364	150–300	0.2 (170)	LIR (985/874 nm)	58
[Nd(TTA)₃(MeOH)₂]·0.5Azo-py (A)	Molecular (mononuclear complex)	O₈	360	10–300	<0.1 (300)	LIR (905/880 nm)	55
[Nd(TTA)₃(MeOH)₂]·0.5Azo-py (A)	Molecular (mononuclear complex)	O₈	392	75–300	<0.1 (300)	LIR (905/880 nm)	55
[Nd^III2(valdien)₂(acac)₂]	Molecular (dinuclear complex)	N₃O₅	390	10–330	0.3 (80)	LIR (1045/1058 nm)	59
[Nd^III2(valdien)₂(NO₃)₂]	Molecular (dinuclear complex)	N₃O₅	390	10–330	0.5 (40)	LIR (1020/1105 nm)	59
[Nd(L)(NO₃)₃] (**1Nd**)	Molecular (mononuclear complex)	N₆O₆	804	298–333	0.5 (293)	Intensity (1065 nm)	This work.
[(Nd(L)(NO₃)₂)(μ-BDC)(NO₃)₂]·H₂O (**2Nd**)	Molecular (dinuclear complex)	N₆O₄	804	298–333	0.9 (293)	Intensity (1065 nm)	This work.
[(Nd(L)(NO₃)₂)(μ-BDC)(NO₃)₂]·H₂O (**2Nd**)	Molecular (dinuclear complex)	N₆O₄	804	298–333	0.1 (293)	LIR (1065/1340 nm)	This work.
[(Nd(L)(μ-BTC)(H₂O)₆]·35H₂O (**6Nd**)	Molecular (hexanuclear complex)	N₆O₄	804	298–333	2.4 (293)	LIR (Stark components of 1065 nm)	This work.

The atoms of first coordination sphere and the excitation wavelength used in each example are also presented.
Phen phenantroline, *TTA* thenoyl(trifluoro)acetonate, *Azo-py* 4,4'-azopyridine, *L* Macrociclic ligand used in the present work, *BDC* bencenedicarboxylate, *BTC* bencenetricarboxylate.

splitting of the $^4F_{3/2} \rightarrow {}^4I_{11/2}$ signal (Fig. S10b). The number of doublets in each cluster is different for **1Nd**, presenting two groups of three doublets each in comparison to **2Nd** and **6Nd**, where the lower cluster has two states and the upper has four (see the calculated splitting of 4I₁₁/₂ in Fig. 6). Thus, the emission to one of the clusters can be turned off to separate their contribution to the total emission. Figure S10b shows that both clusters are associated with only one peak, suggesting that the observed splitting in the $^4F_{3/2} \rightarrow {}^4I_{11/2}$ signal reflects the energy pattern of the $^4I_{11/2}$ multiplet instead of $^4F_{3/2}$.

While the shape of the $^4F_{3/2} \rightarrow {}^4I_{11/2}$ emission depends on the $^4I_{11/2}$ splitting, the thermal behavior depends on the relative separation of the Γ and Γ' doublets, which can be described by a Boltzmann distribution (Eq. S6).

Despite the clear evidence of anti-thermal quenching behavior in this series of compounds (Figs. 3 and S7), as evidenced by the sum of the A_1 and A_2 components in Fig. S8, the trend of these components in the **6Nd** compound differs from the **1Nd** and **2Nd** samples. A plausible explanation is that the A_2 (Fig. S8e) component predominantly originates from the emission of the higher Stark component of the $^4F_{3/2}$ to upper Stark components of the $^4I_{11/2}$ level, as shown by the σ_2 line in Fig. 6. Conversely, the A_1 (Fig. S8e) is primarily associated with the emission from the lower Stark component of the $^4F_{3/2}$ (σ_1 line in Fig. 6), exhibiting thermal behavior similar to that observed for the $^5D_4 \rightarrow {}^7F_5$ emission in Tb^III-based silsesquioxanes with acetylacetonate as antenna L[54].

Furthermore, the anti-thermal quenching effect across all samples leads to an increase in the population of the $^4F_{3/2}$ level. Without accounting for the increase in the $^4F_{3/2}$ population (i.e., the population is maintained constant), the variation in the populations of the upper (Γ') and lower (Γ) Stark levels of $^4F_{3/2}$ with temperature can be estimated using Eq. S6 and is illustrated in Fig. 7 (empty symbols). Under this condition, the sum of the empty symbols equals 1 (normalized population). However, the anti-thermal quenching effect causes the $^4F_{3/2}$ population to increase (full symbols in Fig. 6). Consequently, when the 4F₃/₂ population increases due to anti-thermal quenching, the total relative population grows such that $\eta(\Gamma') + \eta(\Gamma) \geq 1$, reflecting the trend observed in Fig. S8e.

Regarding the thermal behavior of **1Nd** and **2Nd** compounds, it is reasonable that their emissions components originate from the same Stark components of $^4F_{3/2}$ (Γ or Γ', as illustrated in Fig. 6), which explains their similar trend with temperature and relative low thermometric performance in comparison with **6Nd**.

Based on the theoretical framework for ratiometric single-ion thermometers by Suta and Meijerink[56], and the calculated CASSCF energy gap between Γ and Γ' for each compound, we can estimate the response function $\rho(T)$, Fig. 8, normalized to the most responsive temperature[56]. This response function can be derived as:

$$\rho(T) = \frac{1}{4}\left(\frac{\delta}{k_B \cdot T}\right)^2 e^{\left(2 - \frac{\delta}{k_B \cdot T}\right)} \tag{1}$$

where k_B and T are the Boltzmann constant and temperature.

As expected for single-ion luminescent thermometers based on the ratio between two Stark components of lanthanide ions, all three compounds exhibit improved performance in the cryogenic temperature range[54,56], as indicated by the $\rho(T)$ trend in Fig. 8. However, these molecular thermometers may not achieve optimal sensitivity at cryogenic temperatures, as the anti-thermal quenching effect is not considered in the $\rho(T)$ formulation, and this effect may not be evident at low temperatures. This is because at cryogenic temperatures, the population dynamics—specifically the thermal population of excited states—are less effective, resulting in a reduced anti-thermal quenching effect compared to higher temperatures. Nonetheless, the larger δ calculated in **6Nd** corroborates that this compound offers superior temperature response within the physiological temperature range compared to the others.

Concerning the anti-thermal quenching behavior, there are two reasons for the outperformance of 6Nd complex against 1Nd and 2Nd: L field
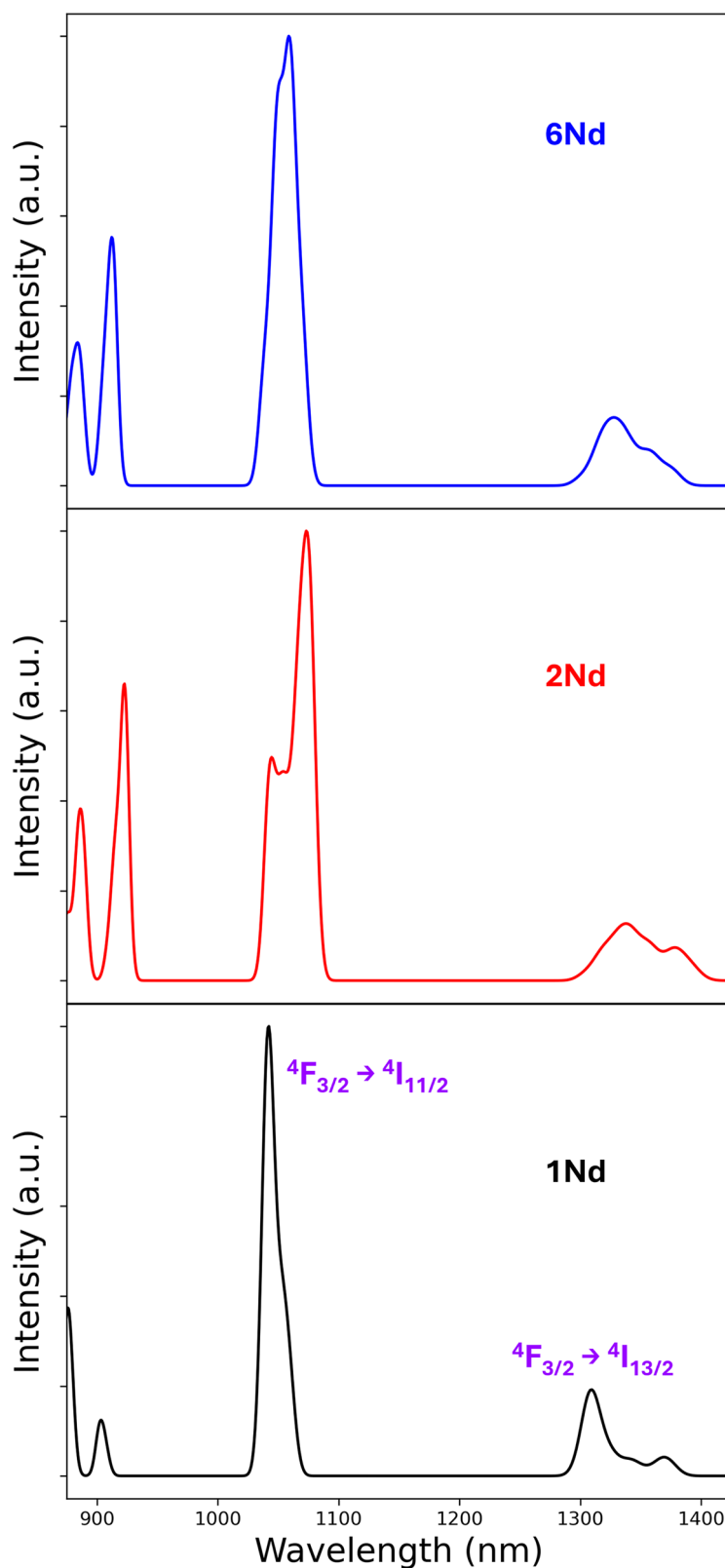
Fig. 5 | CASSCF(3,12) calculated emission profiles of Nd^{III} complexes. Spectra are shown for **1Nd** (bottom, black), **2Nd** (middle, red), and **6Nd** (top, blue) complexes.

effects and multiphonon decay. The stronger L field in 6Nd results in a greater splitting of the $^4F_{3/2}$ energy level (Fig. 6), which extends the thermometer response function $\rho(T)$ to higher temperature ranges compared to 1Nd and 2Nd (Fig. 8).

The energy gap between the $^4F_{5/2}$ and $^4F_{3/2}$ states is about 1000 cm^{-1}[57], a value that can be easily bridged by phonons. Consequently, the $^4F_{5/2} \rightsquigarrow ^4F_{3/2}$ multiphonon process is more effective in 6Nd. This is probably due to the high number of vibrational modes available and confirmed by the

Fig. 6 | Dieke diagram for 6Nd with the calculated emission spectrum, and the specific Stark splitting for the studied complexes. δ represents the calculated Stark splitting (in cm^{-1}) between the two doublets Γ and Γ' of the $^4F_{3/2}$ level, used for the Boltzmann distribution. σ_1 and σ_2 denote the wavenumbers of the lower and higher energy bands, respectively, as determined from band deconvolutions in Fig. S6.
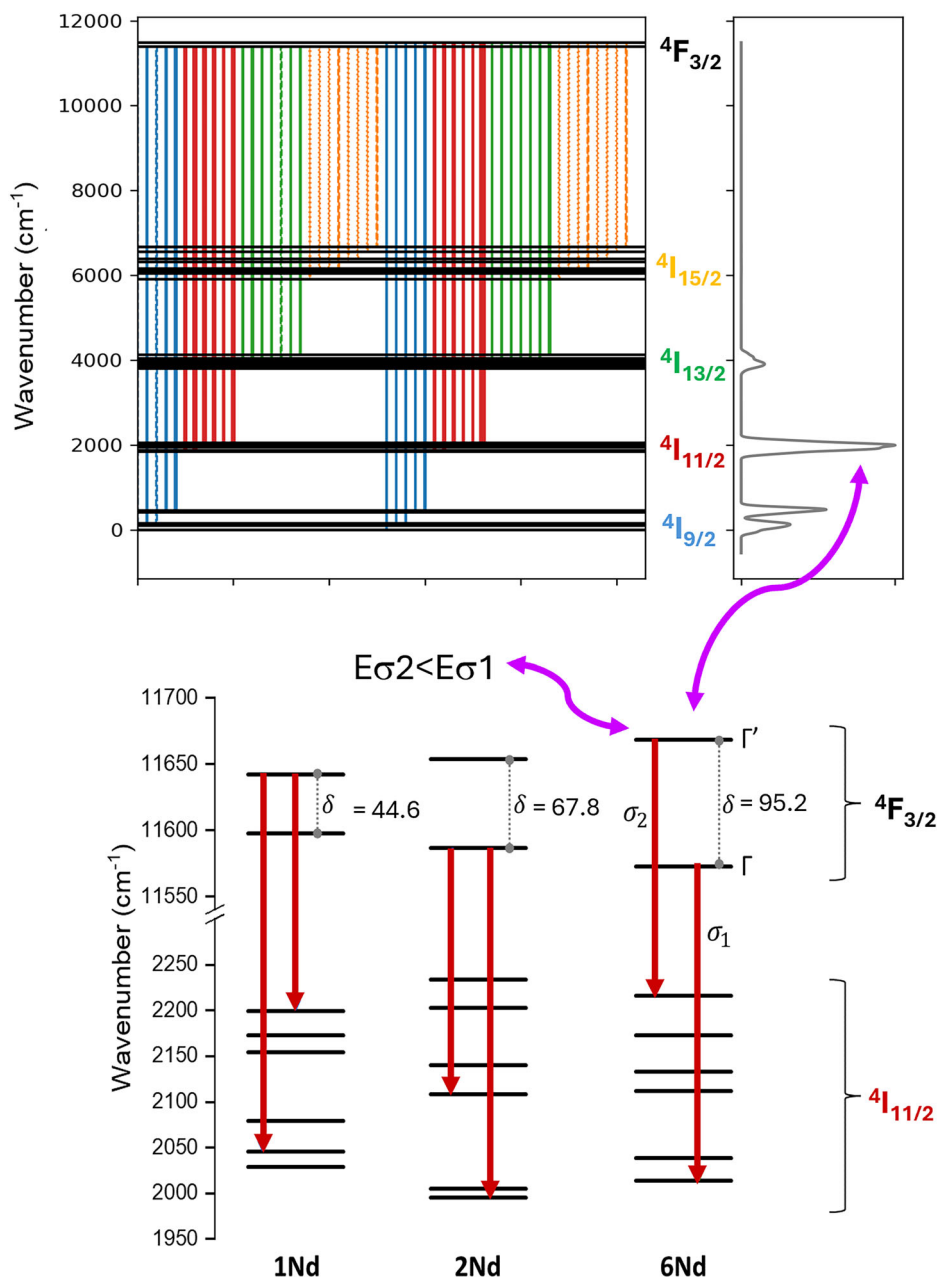
decrease in the intensity of the $^4F_{5/2} \rightarrow {}^4I_{11/2}$ (this is also observed for the $^4F_{5/2} \rightarrow {}^4I_{13/2}$) transition with increasing temperature (Fig. 3c), suggesting that the population of the $^4F_{5/2}$ state decreases via multiphonon relaxation, which leads to an increased population of the $^4F_{3/2}$ state. This behavior, where the $^4F_{5/2}$ population decreases with temperature, is not observed in 1Nd and 2Nd (Fig. S7).

Conclusion

Three distinct molecular complexes incorporating the Nd^{III} cation and a macrocyclic L derived from 2,6-pyridinedicarbaldehyde and ethylenediamine were synthesized. The introduction of bridging L, specifically 1,4-benzenedicarboxylate (BDC) and 1,3,5-benzenetricarboxylate (BTC) ions, facilitated the formation of novel polymetallic species. With BDC as the auxiliary L, a dinuclear complex was formed, wherein DBC bridged two mononuclear units, replacing two nitrate L with carboxylate groups. When BTC was employed as the linker, a hexanuclear cyclic compound was produced, featuring a complete substitution of nitrate L with BTC's carboxylate groups. Direct excitation of the Nd^{III} ion at 804 nm enabled the

monitoring of its emission within the second biological window. Complex 6Nd emerged as the most sensitive with an LIR of the two Stark components of the $^4F_{3/2} \rightarrow {}^4I_{11/2}$ transition, achieving a sensitivity (S$_r$) of 2.4%·K^{-1} at 293 K, surpassing that of complexes 1Nd and 2Nd. This indicates that optimizing the first coordination sphere and the nuclearity/connectivity of emitting systems can significantly enhance the thermometric performance of Nd^{III} molecular complexes.

The comprehensive theoretical analysis of compounds 1Nd, 2Nd, and 6Nd provides an insightful understanding of their emission characteristics and thermal behavior. The calculated CASSCF emission spectra reveal a clear dependence on the coordination environment and electronic structure, with notable differences in the $^4F_{3/2} \rightarrow {}^4I_{11/2}$ transition.

For 1Nd and 2Nd, the observed two-peak emission pattern reflects the distinct contributions from lower and higher energy Kramers' doublets of the $^4F_{3/2}$ multiplet, aligned with the calculated splitting of the $^4I_{11/2}$ multiplet. In contrast, 6Nd demonstrates a merged single peak, suggesting a different emission profile primarily influenced by the $^4I_{11/2}$ multiplet's splitting rather than the $^4F_{3/2}$.
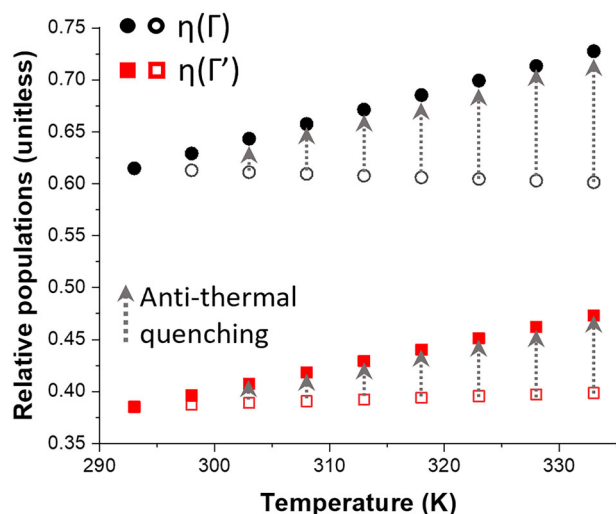
Fig. 7 | Temperature-dependent Boltzmann populations. Boltzmann populations of the Kramer's doublets of $^4F_{3/2}$ (Γ and Γ') for **6Nd**, showing the population distribution without considering the anti-thermal quenching effect (empty symbols) where the sum of populations is constant, and with the anti-thermal quenching effect, which causes an increase in the overall $^4F_{3/2}$ population with temperature (full symbols). The trend is consistent with the observed in Fig. S8e.
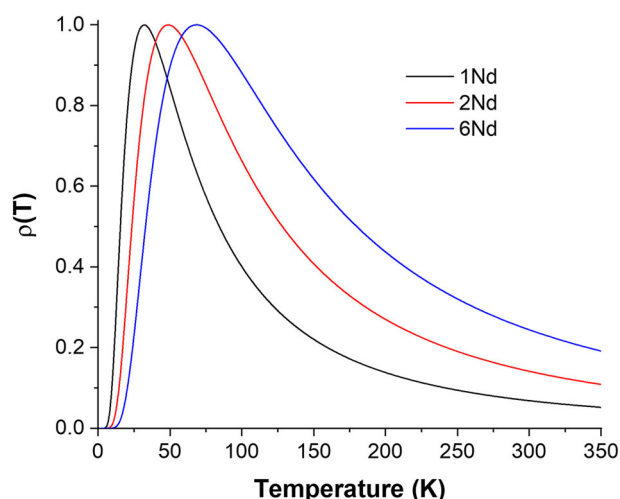

Fig. 8 | Thermal response profiles of compounds. Normalized response function $\rho(T)$ for the compounds **1Nd (black)**, **2Nd (red)**, and **6Nd (blue)**.

Thermal behavior analysis indicates an anti-thermal quenching effect across all samples, impacting the relative populations of the Kramers' doublets. Notably, the compound **6Nd** stands out with a larger $^4F_{3/2}$ splitting, translating to superior sensitivity within the physiological temperature range. This highlights its potential for enhanced performance in temperature-sensitive applications.

Overall, the results underscore the significance of electronic structure and thermal effects in tuning the emission properties of Nd^{III}-based compounds. Specifically, the **6Nd** improved temperature response positioning it as a promising candidate for applications requiring precise thermal sensing, particularly in physiological contexts.

Data availability
CCDC2284360 for **1Nd**, CCDC2284362 for **2Nd**, and CCDC2295992 for **6Nd** contain the supplementary crystallographic data for this paper. These data can be obtained free of charge via www.ccdc.cam.ac.uk/data_request/cif, by emailing data_request@ccdc.cam.ac.uk, or by contacting The Cambridge

Crystallographic Data Center, 12 Union Road, Cambridge CB2 1EZ, UK; fax: +44 1223 336033. All spectroscopic data are available at https://doi.org/10.6084/m9.figshare.28824833.

References
1. Cheshire, W. P. Thermoregulatory disorders and illness related to heat and cold stress. *Auton. Neurosci.* **196**, 91–104 (2016).
2. Corredoira-Vázquez, J. et al. Synthesis and applications of lanthanoid complexes of pentadentate and hexadentate N_5 and N_6 macrocycles: a review. *J. Rare Earths* **42**, 1–15 (2024).
3. Gil, Y., Castro-Alvarez, A., Fuentealba, P., Spodine, E. & Aravena, D. Lanthanide SMMs based on belt macrocycles: recent advances and general trends. *Chem. Eur. J.* **28**, e202200336 (2022).
4. Larionova, J., Guari, Y., Sene, S. & Félix, G. Luminescent lanthanide-based single-molecule magnets. In *Handbook on the Physics and Chemistry of Rare Earths* 93–173 (Elsevier, 2023)
5. Pellissier, H. Recent developments in enantioselective lanthanide-catalyzed transformations. *Coord. Chem. Rev.* **336**, 96–151 (2017).
6. Hernández-Rodríguez, M. A. et al. Designing all-photonic molecular analogs for electrical components: a reprogrammable luminescent filter based on Ln^{3+} ions. *Laser Photon. Rev.* **17**, 2200877 (2023).
7. Gálico, D. A., Santos Calado, C. M. & Murugesu, M. Lanthanide molecular cluster-aggregates as the next generation of optical materials. *Chem. Sci.* **14**, 5827–5841 (2023).
8. Wybourne, B. G. *Spectroscopic Properties of Rare Earths* (John Wiley & Sons, 1965).
9. Igoa, F., Peinado, G., Suescun, L., Kremer, C. & Torres, J. Design of a white-light emitting material based on a mixed-lanthanide metal organic framework. *J. Solid State Chem.* **279**, 120925 (2019).
10. Wade, S. A., Muscat, J. C., Collins, S. F. & Baxter, G. W. Nd^{3+}-doped optical fiber temperature sensor using the fluorescence intensity ratio technique. *Rev. Sci. Instrum.* **70**, 4279–4282 (1999).
11. Puccini, A., Liu, N. & Hemmer, E. Lanthanide-based nanomaterials for temperature sensing in the near-infrared spectral region: illuminating progress and challenges. *Nanoscale* **16**, 10975–10993 (2024).
12. Cantarano, A. et al. Autofluorescence-free in vivo imaging using polymer-stabilized Nd^{3+}-doped YAG nanocrystals. *ACS Appl. Mater. Interfaces* **12**, 51273–51284 (2020).
13. Hemmer, E., Benayas, A., Légaré, F. & Vetrone, F. Exploiting the biological windows: current perspectives on fluorescent bioprobes emitting above 1000 nm. *Nanoscale Horiz.* **1**, 168–184 (2016).
14. Suta, M. et al. Making Nd^{3+} a sensitive luminescent thermometer for physiological temperatures—an account of pitfalls in Boltzmann thermometry. *Nanomaterials* **10**, 543 (2020).
15. Back, M., Xu, J., Ueda, J. & Tanabe, S. Neodymium(III)-doped Y$_3$Al$_2$Ga$_3$O$_{12}$ garnet for multipurpose ratiometric thermometry: from cryogenic to high temperature sensing. *J. Ceram. Soc. Jpn.* **131**, 22167 (2023).
16. Brites, C. D. S. et al. Spotlight on luminescence thermometry: basics, challenges, and cutting-edge applications. *Adv. Mater.* **35**, 2302749 (2023).
17. Skripka, A., Morinvil, A., Matulionyte, M., Cheng, T. & Vetrone, F. Advancing neodymium single-band nanothermometry. *Nanoscale* **11**, 11322–11330 (2019).
18. Wawrzynczyk, D., Bednarkiewicz, A., Nyk, M., Strek, W. & Samoc, M. Neodymium(III) doped fluoride nanoparticles as non-contact optical temperature sensors. *Nanoscale* **4**, 6959–6961 (2012).
19. Benayas, A. et al. Nd:YAG near-infrared luminescent nanothermometers. *Adv. Opt. Mater.* **3**, 687–694 (2015).
20. Zhao, D. et al. A highly sensitive near-infrared luminescent metal-organic framework thermometer in the physiological range. *Chem. Commun.* **52**, 8259–8262 (2016).

21. Nunes, L. A. O., Souza, A. S., Carlos, L. D. & Malta, O. L. Neodymium doped fluoroindogallate glasses as highly-sensitive luminescent non-contact thermometers. *Opt. Mater.* **63**, 42–45 (2017).

22. Blois, L. et al. Unusually large ligand field splitting in anionic europium(III) complexes induced by a small imidazolic counterion. *Inorg. Chem.* **63**, 16861–16871 (2024).

23. Brites, C. D. S., Millán, A. & Carlos, L. D. Lanthanides in luminescent thermometry. *Handb. Phys. Chem. Rare Earths* **49**, 339–427 (2016).

24. Oggianu, M. et al. Insights into Nd^{III} to Yb^{III} energy transfer and its implications in luminescence thermometry. *Chem. Mater.* **36**, 3452–3463 (2024).

25. Trannoy, V., Carneiro Neto, A. N., Brites, C. D. S., Carlos, L. D. & Serier-Brault, H. Engineering of mixed Eu^{3+}/Tb^{3+} metal-organic frameworks luminescent thermometers with tunable sensitivity. *Adv. Opt. Mater.* **9**, 2001938 (2021).

26. Wei, Y. et al. Tunable anti-thermal quenching luminescence of Eu^{3+}-doped metal-organic framework and temperature-dependent photonic coding. *Adv. Funct. Mater.* **34**, 2401664 (2024).

27. Wei, Y. et al. Frenkel defect-modulated anti-thermal quenching luminescence in lanthanide-doped $Sc_2(WO_4)_3$. *Angew. Chem. Int. Ed.* **62**, e202303482 (2023).

28. Fuentealba, P. et al. Thermal dependence of the luminescent properties of mononuclear Tb^{III} macrocyclic complexes. *Eur. J. Inorg. Chem.* **2021**, 4543–4551 (2021).

29. Gil, Y. et al. Dual visible and near-infrared luminescence in mononuclear macrocyclic erbium(III) complexes via ligand and metal centred excitation. *Dalton Trans.* **52**, 3158–3168 (2023).

30. Gil, Y., Fuentealba, P., Vega, A., Spodine, E. & Aravena, D. Control of magnetic anisotropy by macrocyclic ligand distortion in a family of Dy^{III} and Er^{III} single molecule magnets. *Dalton Trans.* **49**, 17709–17718 (2020).

31. Kumar, D. S. & Alexander, V. Macrocyclic complexes of lanthanides in identical ligand frameworks part 1. Synthesis of lanthanide(III) and yttrium(III) complexes of an 18-membered dioxatetraaza macrocycle. *Inorg. Chim. Acta* **238**, 63–71 (1995).

32. Bruker, APEX2, SAINT & SADABS. Bruker AXS Inc. Madison, Wisconsin, USA (2012).

33. Sheldrick, G. M. Crystal structure refinement with SHELXL. *Acta Crystallogr. C Struct. Chem.* **71**, 3–8 (2015).

34. Spek, A. L. Platon squeeze: A tool for the calculation of the disordered solvent contribution to the calculated structure factors. *Acta Crystallogr. C Struct. Chem.* **71**, 9–18 (2015).

35. Van Der Sluis, P. & Spek, A. L. BYPASS: an effective method for the refinement of crystal structures containing disordered solvent regions. *Acta Crystallogr. Sect. A* **46**, 194–201 (1990).

36. Westrip, S. P. PublCIF: software for editing, validating and formatting crystallographic information files. *J. Appl. Crystallogr.* **43**, 920–925 (2010).

37. Neese, F. Software update: the ORCA program system—version 5.0. *Wiley Interdiscip. Rev. Comput. Mol. Sci.* **12**, 1–15 (2022).

38. Malmqvist, P. Å. & Roos, B. O. The CASSCF state interaction method. *Chem. Phys. Lett.* **155**, 189–194 (1989).

39. Nakajima, T. & Hirao, K. The Douglas–Kroll–Hess approach. *Chem. Rev.* **112**, 385–402 (2012).

40. Weigend, F., Ahlrichs, R. & Gmbh, F. K. Balanced basis sets of split valence, triple zeta valence and quadruple zeta valence quality for H to Rn: design and assessment of accuracy. *Phys. Chem. Phys.* **7**, 3297–3305 (2005).

41. Aravena, D., Neese, F. & Pantazis, D. A. Improved segmented all-electron relativistically contracted basis sets for the lanthanides. *J. Chem. Theory Comput.* **12**, 1148–1156 (2016).

42. Aravena, D., Atanasov, M. & Neese, F. Periodic trends in lanthanide compounds through the eyes of multireference ab initio theory. *Inorg. Chem.* **55**, 4457–4469 (2016).

43. Richardson, F. S., Reid, M. F., Dallara, J. J. & Smith, R. D. Energy levels of lanthanide ions in the cubic $Cs_2NaLnCl_6$ and Cs_2NaYCl_6:Ln^{3+} (doped) systems. *J. Chem. Phys.* **83**, 3813–3830 (1985).

44. Longhi, G., Castiglioni, E., Abbate, S., Lebon, F. & Lightner, D. A. Experimental and calculated CPL spectra and related spectroscopic data of camphor and other simple chiral bicyclic ketones. *Chirality* **25**, 589–599 (2013).

45. Gendron, F. et al. Ab initio study of circular dichroism and circularly polarized luminescence of spin-allowed and spin-forbidden transitions: from organic ketones to lanthanide complexes. *J. Chem. Theory Comput.* **15**, 4140–4155 (2019).

46. Perdew, J. P. Density-functional approximation for the correlation energy of the inhomogeneous electron gas. *Phys. Rev.* **33**, 8822–8824 (1986).

47. Becke, A. D. Density-functional exchange-energy approximation with correct asymptotic behavior. *Phys. Rev.* **38**, 3098–3100 (1988).

48. Andrae, D., Häußermann, U., Dolg, M., Stoll, H. & Preuß, H. Energy-adjusted ab initio pseudopotentials for the second and third row transition elements. *Theor. Chim. Acta* **77**, 123–141 (1990).

49. SHAPE v2.1, Continuous Shape Measures Calculation (2013).

50. Lou, X. et al. Capacity control of ferric coordination polymers by zinc nitrate for lithium-ion batteries. *RSC Adv.* **6**, 86126–86130 (2016).

51. Alammar, T. et al. Luminescence properties of mechanochemically synthesized lanthanide containing MIL-78 MOFs. *Dalton Trans.* **47**, 7594–7601 (2018).

52. da Gama, A. A. S., de Sá, G. F., Porcher, P. & Caro, P. Energy levels of Nd^{3+} in $LiYF_4$. *J. Chem. Phys.* **75**, 2583–2587 (1981).

53. Trejgis, K., Ledwa, K., Maciejewska, K., Li, L. & Marciniak, L. Modulation of thermometric performance of single-band-ratiometric luminescent thermometers based on luminescence of Nd^{3+} activated tetrafluorides by size modification. *Sci. Rep.* **12**, 5847 (2022).

54. Félix, G. et al. Luminescent Ln^{3+}-based silsesquioxanes with a β-diketonate antenna ligand: toward the design of efficient temperature sensors. *Front. Chem.* **12**, 1–14 (2024).

55. Kumar, K. et al. Neodymium β-diketonate showing slow magnetic relaxation and acting as a ratiometric thermometer based on near-infrared emission. *RSC Adv.* **9**, 23444–23449 (2019).

56. Suta, M. & Meijerink, A. A theoretical framework for ratiometric single ion luminescent thermometers—thermodynamic and kinetic guidelines for optimized performance. *Adv. Theory Simul.* **3**, 2000176 (2020).

57. Carnall, W. T., Crosswhite, H. & Crosswhite, H. M. *Energy Level Structure and Transition Probabilities in the Spectra of the Trivalent Lanthanides in LaF_3. Energy.* Report No. TRN: 79-005910 (Argonne National Lab, 1978)

58. Kumar, K., Stefanczyk, O., Nakabayashi, K., Mineo, Y. & Ohkoshi, S. I. Development of Nd (III)-based terahertz absorbers revealing temperature dependent near-infrared luminescence. *Int. J. Mol. Sci.* **23**, 6051 (2022).

59. Bispo-Jr, A. G. et al. The role of terminal ligands in the slow relaxation of magnetisation and luminescence thermometry of dinuclear Nd^{III} complexes. *Inorg. Chem. Front.* **10**, 3929–3939 (2023).

Acknowledgements

Author contributions

The manuscript was written through contributions of all authors. All authors have given approval to the final version of the manuscript. Investigation and data curation: M.J.M., P.F.C., and Y.G. Formal analysis, writing, review, and editing: A.V. and R.C. de S. Writing, review, and editing: C.D.S.B., L.D.C., and F.V. Conceptualization, formal analysis, and writing-review-editing: D.A., A.N.C.N., and P.F.

Competing interests

The authors declare no competing interests.

Additional information

Supplementary information The online version contains supplementary material available at
https://doi.org/10.1038/s42004-025-01536-9.

Correspondence and requests for materials should be addressed to Daniel Aravena, Albano N. Carneiro Neto or Pablo Fuentealba.

Peer review information *Communications Chemistry* thanks the anonymous reviewers for their contribution to the peer review of this work.

Reprints and permissions information is available at
http://www.nature.com/reprints